PHYSICS

Spin Hall effect of transversely spinning light

Liang Peng[1,2]*†, Hang Ren[3]†, Ya-Chao Liu[4]†, Tian-Wei Lan[2], Kui-Wen Xu[2], De-Xin Ye[5], Hong-Bo Sun[3,6], Su Xu[3]*, Hong-Sheng Chen[7], Shuang Zhang[8,9]*

Light carries spin angular momentum, which, in the free space, is aligned to the direction of propagation and leads to intriguing spin Hall phenomena at an interface. Recently, it was shown that a transverse-spin (T-spin) state could exist for surface waves at an interface or for bulk waves inside a judiciously engineered metamaterial, with the spin oriented perpendicular to the propagation direction. Here, we demonstrate the spin Hall effect for transversely spinning light—a T-spin–induced beam shift at the interface of a metamaterial. It is found that the beam shift takes place in the plane of incidence, in contrast to the well-known Imbert-Fedorov shifts. The observed T-spin–induced beam shift is of geometrodynamical nature, which can be rendered positive or negative controlled by the orientation of T-spin of the photons. The unconventional spin Hall effect of light found here provides a previously unexplored mechanism for manipulating light-matter interactions at interfaces.

INTRODUCTION

Spin-orbit interaction (SOI) is a universal phenomenon that is prevalent in various research areas including condensed matter physics (*1*, *2*) and photonics (*3*–*5*). Because of SOI of light, the spatial degrees of freedom of a light beam couple with its circular polarization, i.e., optical spin (*6*–*8*). Besides its fundamental importance (*9*–*11*), optical SOI has triggered many novel applications, with some representative examples including spin-to-orbital angular momentum conversion (*6*, *12*, *13*), spin-to-vortex conversion (*14*, *15*), photonic topological insulators (*16*–*18*), spin-controlled unidirectional propagation of electromagnetic (EM) modes (*19*–*22*), and spin Hall effect of light (SHEL) (*23*–*28*).

SHEL, spin-dependent shift of the reflected or refracted beam for a circularly polarized incident laser beam, is one of the most fundamental optical processes universally present in various optical systems (*23*–*28*). In conventional media, light has a longitudinal angular momentum, i.e., it is aligned with its linear momentum ($\bar{k}$) (*3*, *5*). SHEL refers to a spin-dependent lateral shift of the refracted/reflected beam in a direction normal to the plane of incidence (*27*–*29*). This effect, named the Imbert-Fedorov (I-F) shift (Fig. 1, A and B), can be attributed to the internal Berry phase associated with the reflection and refraction processes (*5*). It was recently demonstrated that the spin angular momentum (SAM) of light can be transverse to its propagation, i.e., the rotation of electric or magnetic field can take place in a plane that contains the propagation direction [i.e., the transverse-spin (T-spin)] (*30*–*32*). The T-spin of light has been observed in diverse systems, including evanescent waves near optical interfaces (*30*) and inside carefully designed inhomogeneous structures (*31*, *32*), spatially structured propagating waves (*33*, *34*), and bulk modes inside a judiciously engineered metamaterial (MM) with magnetoelectric (ME) coupling (*35*). T-spin light shows some markedly different behaviors from light with conventional longitudinal spin, such as wheel-like dynamics of optical fields (*4*), twisting of Mie particle in evanescent field (*21*, *36*), and extraordinary optical momentum and force upon internal total reflection (*31*). Here, we demonstrate spin Hall effect for bulk optical mode with T-spin, which is manifested as a beam shift in the plane of incidence (equivalently, in the plane of the rotating electric or magnetic field). Unlike the well-studied Goos-Hänchen (G-H) shift for linearly polarized waves that rely on the evanescent wave penetration (*27*, *28*), the beam shift studied here is of purely geometrodynamical nature, whose direction and amplitude are solely determined by the SAM of the beam (Fig. 1, C and D).

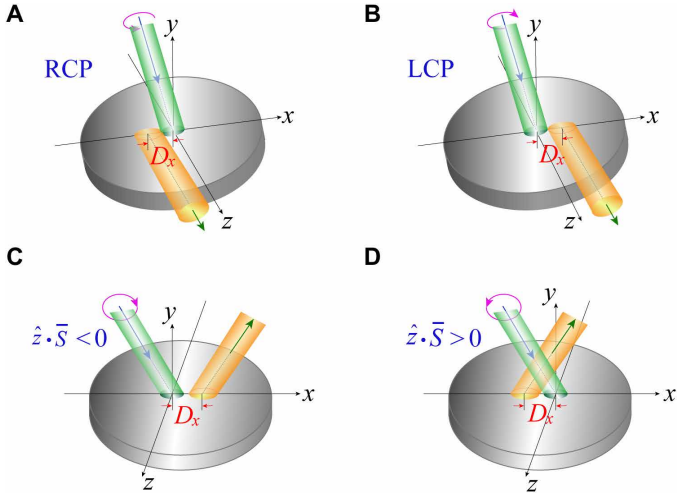

Fig. 1. Spatial shifting of spin polarized light beams. (**A** and **B**) I-F shifts perpendicular to the plane of incidence, for right-handed circular polarization (RCP) (A) and left-handed circular polarization (B) incident beam. (**C** and **D**) Illustration of beam shifts in the plane of incidence for light with transverse SAM, (C) negative shift for $\hat{z}\cdot\bar{S} < 0$ and (D) positive shift for $\hat{z}\cdot\bar{S} > 0$.

[1]School of Information and Electrical Engineering, Zhejiang University City College, Hangzhou, China. [2]School of electronics and information, Hangzhou Dianzi University, Hangzhou, China. [3]State Key Laboratory of Integrated Optoelectronics, College of Electronic Science and Engineering, Jilin University, Changchun, China. [4]Institute of Microscale Optoelectronics, Shenzhen University, Shenzhen, China. [5]Laboratory of Applied Research on Electromagnetics (ARE), Zhejiang University, Hangzhou, China. [6]State Key Laboratory of Precision Measurement Technology and Instruments, Department of Precision Instrument, Tsinghua University, Beijing, China. [7]State Key Laboratory of Modern Optical Instrumentation, Interdisciplinary Center for Quantum Information, College of Information Science and Electronic Engineering, Zhejiang University, Hangzhou, China. [8]Department of Physics, University of Hong Kong, Hong Kong, China. [9]Department of Electrical and Electronic Engineering, University of Hong Kong, Hong Kong, China.
*Corresponding author. Email: pengl@zucc.edu.cn (L.P.); xusu@jlu.edu.cn (S.X.); shuzhang@hku.hk (S.Z.)
†These authors contributed equally to this work.

RESULTS

The T-spin Hall effect

Without losing generality, we consider the total reflection in a medium supporting bulk optical mode with a T-spin. The basic configuration of the system being studied is shown in Fig. 2A, in which the upper half space ($y > 0$) is filled with a bianisotropic medium, while a perfect magnetic conductor (PMC) is assumed for the lower half space ($y < 0$). The bianisotropic medium is described by the constitutive relations of $\overline{B} = \overline{\overline{\mu}} \cdot \overline{H} + i\overline{\overline{\chi}} \cdot \overline{E}$ and $\overline{D} = \overline{\overline{\varepsilon}} \cdot \overline{E} - i\overline{\overline{\chi}}^T \cdot \overline{H}$, with $\overline{\overline{\varepsilon}} = \varepsilon_0 \begin{bmatrix} \varepsilon_1 & 0 & 0 \\ 0 & \varepsilon_2 & 0 \\ 0 & 0 & \varepsilon_3 \end{bmatrix}$, $\overline{\overline{\mu}} = \mu_0 \begin{bmatrix} \mu_1 & 0 & 0 \\ 0 & \mu_2 & 0 \\ 0 & 0 & \mu_3 \end{bmatrix}$, and $\overline{\overline{\chi}} = \sqrt{\varepsilon_0 \mu_0} \begin{bmatrix} 0 & 0 & \chi \\ 0 & 0 & 0 \\ 0 & 0 & 0 \end{bmatrix}$.

For simplicity, the wave propagation is assumed to take place in the x-y plane, and, hence, we have $k_z = 0$. The EM medium described above has a broken mirror symmetry in y direction (the normal of the reflector surface), and it supports bulk mode propagating in the x-y plane with a rotating magnetic field lying in the same plane, corresponding to a transverse SAM in z direction (*30*, *35*, *36*). For the interface formed between the bianisotropic MM and PMC, the incident and reflected waves are linked through the boundary condition of PMC, i.e., zero tangential magnetic field at the interface (*36*, *37*), which leads to the following expression for the reflection coefficient (see Materials and Methods)

$$R = \frac{k\cos\phi_i + ik_0\chi}{k\cos\phi_r - ik_0\chi} \tag{1}$$

with ϕ_i and ϕ_r being the incident and reflection angles, respectively (Fig. 2A). In Eq. 1, $k = \sqrt{k_x^2 + k_y^2}$ and k_0 is the wave number in the free space. Because total reflection is guaranteed by the PMC surface, $|R| \equiv 1$ and R can be simply written as $R = e^{iP(\phi_i, \phi_r)}$.

The elliptically polarized incident and reflected waves can be expressed as $\overline{H}_i = U_i(\hat{x} + \hat{y}A_i e^{iQ_i}) e^{i\overline{k}_i \cdot \overline{r}}$ and $\overline{H}_r = U_r(\hat{x} + \hat{y}A_r e^{iQ_r}) e^{i\overline{k}_r \cdot \overline{r}}$, respectively, wherein $A_{i(r)}$ and $Q_{i(r)}$ are real numbers accounting for the spinning of EM fields (*5*, *30*). After some derivation, we have $R = -e^{i(Q_r - Q_i)}$, which indicates that the phase of reflectance arises from the variation of the polarization state (i.e., exhibiting geometrical nature). Consequently, a spatial shift for a light beam is induced in the plane of incidence, which strongly depends on the SAM of the operation photons, as elaborated below.

For an incident Gaussian beam, the shift of beam center in the x direction can be numerically calculated by $D_x = \frac{dP}{dk_x}$, i.e., the well-known approach in evaluating the shift of light beams (the Artmann formula) (*5*, *27*–*29*). It is straightforward to obtain $\frac{dP}{dk_x} = \frac{dQ_r}{dk_x} - \frac{dQ_i}{dk_x}$, and then D_x can be expressed explicitly in terms of ϕ_i, which yields

$$D_x = 2\frac{k_0}{\cos\phi_i}\frac{\mu_1}{\mu_2}\frac{\chi\sin\phi_i}{k^2\cos^2\phi_i + k_0^2\chi^2} \tag{2}$$

Note that the beam shift D_x is induced by a nonzero bianisotropy term χ, and its sign can be flipped by reversing the bianisotropy ($\chi \to -\chi$), which also leads to the flipping of the SAM of the incident beam for a given incident angle (*35*). Thus, a link is established between the beam shift [as schematically depicted in Fig. 1 (C and D)] upon reflection and the SAM of the incident beam, which is expressed as $\overline{S} = \mathrm{Im}[\mu_0 \overline{H}^* \times \overline{H}]/4\omega$ (*4*). We further define a normalized SAM, which is expressed as

$$\overline{S}^n_{i(r)} = \frac{\overline{S}_{i(r)}}{|H_x|^2} = \hat{z}\frac{-\mu_0}{2c}\frac{\mu_1}{\mu_2}\frac{\chi k\sin\phi_{i(r)}}{k^2\cos^2\phi_{i(r)} + k_0^2\chi^2} \tag{3}$$

with c being the velocity of light in vacuum. For the configuration studied here, we have $\phi_i = \phi_r$, $H_x^i = H_x^r \neq 0$, and thus $\overline{S}_i = \overline{S}_r$, $\overline{S}_i^n = \overline{S}_r^n = \overline{S}^n$. Thus, a simple relationship between the beam shift and normalized SAM can be established

$$D_x = 4c\frac{-k_0}{\mu_0 k\cos\phi_i}(\hat{z} \cdot \overline{S}^n) \tag{4}$$

Note that D_x diverges if $\cos\phi_i$ is sufficiently small, i.e., in the limit of grazing incidence. On the other hand, it is more convenient to experimentally characterize the lateral shift of the beam perpendicular to $\overline{k}_r$ (D_t in Fig. 2A), which is given by

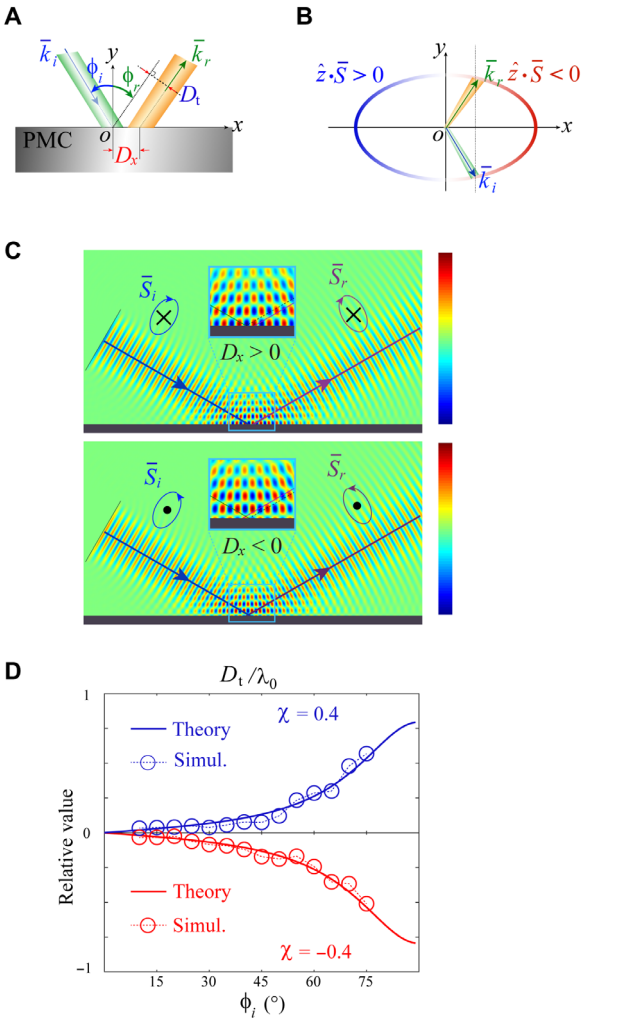

Fig. 2. Spatial shift of transversely spinning beams. (**A**) Systematic configuration of a beam with T-spin reflected by a PMC surface. (**B**) The photon's SAM remains unchanged before and after the interaction with the PMC boundary. (**C**) Full-wave simulations of the beam shift based on the effective medium description. E_z field distribution is plotted, for opposite T-spin cases, in which the light beam experiences a shift in positive or negative directions. In the simulations, $\varepsilon_3 = 2$, $\mu_1 = \mu_2 = 0.6$, and $\chi = \pm 0.4$, for top and bottom panels. The two insets exhibit the field distribution in the enlarged areas. (**D**) Simulated positive and negative beam shifts for incident light with opposite T-spin feature. In (D), λ_0 is the free space wavelength.

$$D_t = D_x \cos\phi_r = -4c\frac{k_0}{\mu_0 k}(\hat{z}\cdot\bar{S}^n) \quad (5)$$

Given that the host medium has isotropic dispersion in the *x*-*y* plane (i.e., $\mu_1 = \mu_2$), D_t would be linearly proportional to $\bar{S}^n$ regardless of the incident angle, i.e., the spin Hall effect is solely determined by the normalized SAM of the incident beam.

To confirm the theoretical predictions, we perform numerical simulations for the beam reflection, using an effective medium description. In Fig. 2C, we plot the electric field (E_z) distributions for the reflection of incident beams with opposite SAMs, wherein the beam centers are indicated by the arrowed lines. In the insets of these two panels, we show the enlarged view of the standing waves close to the PMC surface, which reveals the T-spin–dependent interference pattern upon reflection. We further retrieve the beam shift for different incident angles, and the dependence is plotted in Fig. 2D. It is shown that the beam shift is zero at normal incidence, and it increases with the incident angle because of the increase of the SAM of the beam (the limit at grazing angle is $D_t = \frac{\lambda_0}{\pi\chi}$). For χ of opposite sign (so the SAM of the incident beam is also flipped), the beam shift is reversed, agreeing with the theoretical prediction.

Note that the underlying mechanism of the spin Hall effect of transversely spinning light is very different from the I-F shift. The spin Hall effect of transversely spinning light discussed here is purely induced by the intrinsic property of the bulk optical mode, and it can occur without involving any evanescent waves at the interface. However, the I-F shifts cannot occur in a total reflection if the evanescent wave is absent. As an example, for a beam reflected by a PMC [or perfect electric conductor (PEC)], the reflectance is constant (1 or −1) for both the transverse electric (TE) and transverse magnetic (TM) polarizations, regardless of the incident angle. In addition, in the I-F shifts, the total optical angular momentum around the surface normal (*y* axis) is conserved because of rotational symmetry. However, in the present case, the optical angular momentum around the *z* axis is not conserved, because there exists a torque on the reflective surface, transferring angular momentum between light and the bulk material.

Experiments

The structural design of the MM used in the experiments is shown in Fig. 3A. The detailed information can be found in Materials and Methods. The MM behaves as a homogeneous bianisotropic effective medium away from its resonance frequencies. From full-wave simulations, we can obtain the equifrequency contours for the TE mode in the *x*-*y* plane, as shown in Fig. 3B. The MM exhibits isotropic EM responses in the frequency range from 9.5 to 10.5 GHz. Because the periodicity of the MM (3 mm) is much smaller than the free space wavelength (typically 30 mm at 10 GHz), the effective constitutive parameters (for the TE mode) are well defined (Fig. 3C).

In the experiments, a large area sample in the shape of two quarter disks of different radii (R_1 = 60 cm and R_2 = 90 cm) joined together is fabricated (Fig. 4, A and B). The EM wave is launched from the smaller quarter circle and detected at the edge of the bigger one, with the blue and green arrows indicating the propagation path of the light beams. Here, the small radius of the quarter circle on the incident side can help minimize the broadening of incident EM beam, while the large radius of the quarter circle on the receiving side can effectively reduce the edge effect.

To provide the PMC-like boundary condition in the experiments, an auxiliary MM [artificial magnetic reflector (AMR)] having ultrastrong

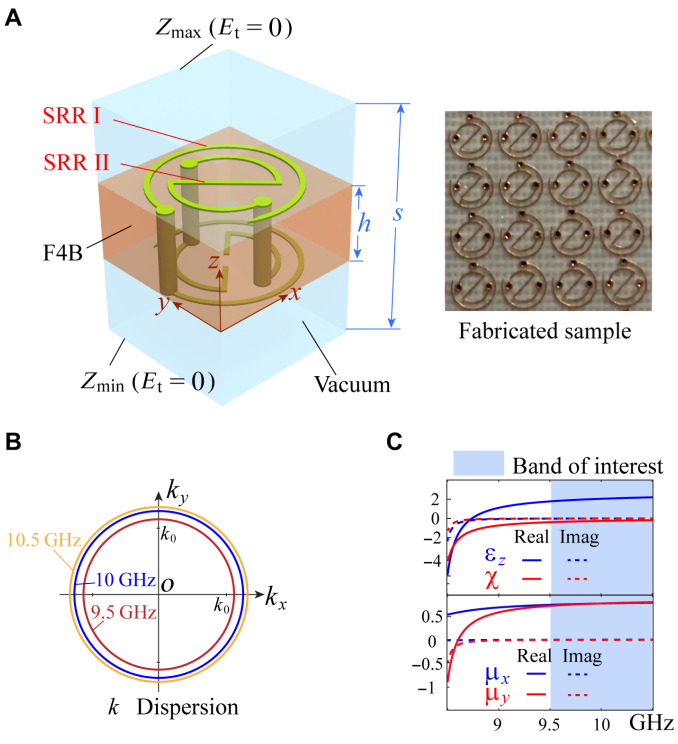

Fig. 3. The design of bianisotropic MM supporting T-spin states. (**A**) Structural configuration of the unit cell with geometric parameters being indicated. (**B**) Numerically calculated equifrequency contours in the k_x-k_y plane. (**C**) Effective constitutive parameters of the MM, which are obtained through the medium parameter retrieval method (*43*–*46*), with applying reflection/transmission coefficients. Real: real part; Imag: imaginary part. The equifrequency contour (B) is calculated with using these parameters.

magnetic resonance around 9.75 GHz is designed. The details of the design and effective parameters of the AMR are provided in Materials and Methods. Such an MM behaves nearly the same as an ideal PMC in the frequency range from 9.65 to 9.85 GHz, which falls in the working band of the bianisotropic MM (9.5 to 10.5 GHz), facilitating the observation of the pronounced beam shift. On the basis of the retrieved effective parameters of the designed MM sample (Fig. 3C), we can numerically evaluate the normalized beam shift, which is shown in Fig. 4C.

For the experimental investigation, the measured D_t shows sensitivity to some experimental imperfections such as systematic uncertainties and material defects and is disturbed. Fortunately, the difference in the beam shifts between incident beams with opposite SAMs, i.e., $\Delta_t = D_t^{\chi} - D_t^{-\chi}$, performs much more stable than D_t^{χ} (or $D_t^{-\chi}$) alone, even with some inevitable imperfections. Proofs can be found in Materials and Methods. As an effective parameter in confirming the beam shifting phenomenon, Δ_t is extracted from the measured data and shown in Fig. 4D. Here, only the results in the frequency range between 9.7 and 9.8 GHz are presented, with fully considering the limited bandwidth of the auxiliary AMR. It is found that the envelope of measured Δ_t grows as the incident angle increases, consistent with the theoretical prediction. However, the measured data do not show sufficient smoothness to finely fit the theoretically calculated results, because of the limited samples in the measurements. For the purpose of interpretation, the measured data points of Δ_t are fitted by a polynomial equation of two variables, incident angle and

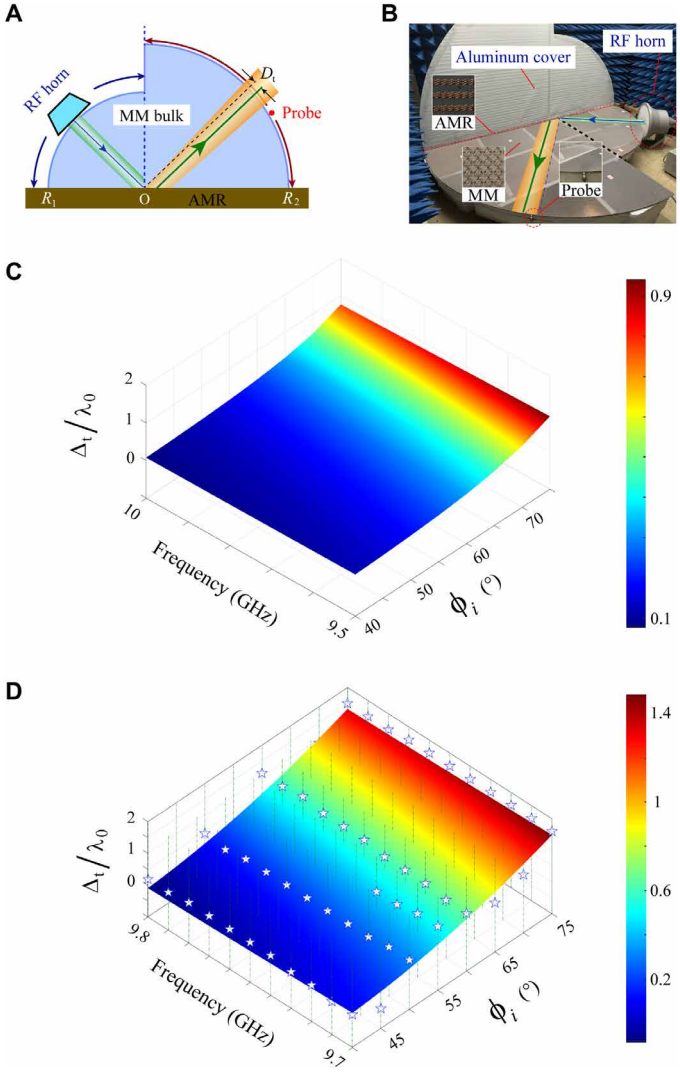

Fig. 4. Experimental demonstration of SHEL for T-spins. (**A**) Schematic configuration of the experimental setup. The AMR layer provides the same boundary condition as a PMC in the frequency range of interest. (**B**) Photo of the experimental setup with light path being indicated. (**C**) Theoretically calculated transverse shift (i.e., $\Delta_t = D_t^{\chi} - D_t^{-\chi}$) as a function of the incident angle and frequency. (**D**) Measured transverse shift (the stars) and the fitted curve. Please note that partial of the stars are hidden behind the fitted curve.

frequency, to illustrate the wideband and wide-angle profile of the beam shifting effect. The fitted surface in Fig. 4D shows good agreement with the simulation results in Fig. 4C. Hence, our measurement provides a direct observation of T-spin–induced SHEL.

DISCUSSION

The observed SHEL by T-spin waves is induced by the evolution of the polarization states (photon spin) inside bianisotropic MMs, which is of purely geometrodynamical nature. The beam shifting is directly determined by the intrinsic SAM of the light beam, i.e., a simple yet elegant link between the beam shift and the light's SAM has been theoretically established. Positive and/or negative beam shifting can be uniquely driven and/or enhanced by the T-spin profile of the bulk's optical mode. The observed phenomenon is physically distinct from the conventional G-H shift for linearly polarized waves (*27*, *28*), which relies on evanescent penetration of the wave into the transmitting medium. The unconventional SHEL found here provides new degrees of freedom for wave manipulation, such as interface optical trapping and particle manipulation (*38*), light position retrieving (*8*), optical sensors (*39*), and edge detectors for imaging (*40*, *41*).

MATERIALS AND METHODS

Reflection of bulk T-spin mode from a PMC surface

We consider the total reflection in a bianisotropic system supporting bulk mode with a T-spin associated with a rotating magnetic field. The basic configuration of the system can be found in Fig. 2A, wherein an infinitely large PMC is assumed in the lower half space, and the upper half space is filled with a bianisotropic medium. Both the eigenstates of the incident and reflected waves have T-spins (for magnetic field) because of the material bianisotropy, but they are generally different because the T-spin is $\bar{k}$ dependent. Here, we consider the reflection by a PMC surface because the transverse spin of the bulk mode inside the bianisotropic MM is associated with the rotating magnetic field.

The constitutive relation can be written in the most general form as $\bar{B} = \bar{\bar{\mu}} \cdot \bar{H} + i\bar{\bar{\chi}} \cdot \bar{E}$ and $\bar{D} = \bar{\bar{\varepsilon}} \cdot \bar{E} - i\bar{\bar{\chi}}^T \cdot \bar{H}$. The spinning bulk mode (magnetic T-spin mode) in the medium can be realized by setting $\bar{\bar{\varepsilon}} = \varepsilon_0 \begin{bmatrix} \varepsilon_1 & 0 & 0 \\ 0 & \varepsilon_2 & 0 \\ 0 & 0 & \varepsilon_3 \end{bmatrix}$, $\bar{\bar{\mu}} = \mu_0 \begin{bmatrix} \mu_1 & 0 & 0 \\ 0 & \mu_2 & 0 \\ 0 & 0 & \mu_3 \end{bmatrix}$, and $\bar{\bar{\chi}} = \sqrt{\varepsilon_0 \mu_0} \begin{bmatrix} 0 & 0 & \chi \\ 0 & 0 & 0 \\ 0 & 0 & 0 \end{bmatrix}$. With such parameters, i.e., ME coupling occurs between E_z and H_x, purely magnetic T-spin mode can be excited (located in the x-y plane).

By solving the source-free Maxwell equations (*42*), we derive the eigenstates of the TE mode ($E_z \neq 0, H_z = 0$) as $\begin{bmatrix} h_x \\ h_y \\ e_z \end{bmatrix} e^{i\bar{k}\cdot\bar{r}} = \begin{bmatrix} \frac{1}{\omega\mu_0\mu_1}(k_y - ik_0\chi) \\ \frac{1}{\omega\mu_0\mu_1}\left(-\frac{\mu_1}{\mu_2}k_x\right) \\ 1 \end{bmatrix} e^{i\bar{k}\cdot\bar{r}}$, with $\frac{\mu_1}{\mu_2}k_x^2 + k_y^2 = k_0^2(\varepsilon_3\mu_1 - \chi^2)$. Then, we can write $\begin{bmatrix} h_x^i \\ h_y^i \\ e_z^i \end{bmatrix} e^{i\bar{k}_i\cdot\bar{r}} = \begin{bmatrix} \frac{1}{\omega\mu_0\mu_1}(k_y^i - ik_0\chi) \\ \frac{1}{\omega\mu_0\mu_1}\left(-\frac{\mu_1}{\mu_2}k_x^i\right) \\ 1 \end{bmatrix} e^{i\bar{k}_i\cdot\bar{r}}$ and $\begin{bmatrix} h_x^r \\ h_y^r \\ e_z^r \end{bmatrix} e^{i\bar{k}_r\cdot\bar{r}} = R \begin{bmatrix} \frac{1}{\omega\mu_0\mu_1}(k_y^r - ik_0\chi) \\ \frac{1}{\omega\mu_0\mu_1}\left(-\frac{\mu_1}{\mu_2}k_x^r\right) \\ 1 \end{bmatrix} e^{i\bar{k}_r\cdot\bar{r}}$ ($\bar{k}_i = \hat{x}k_x^i + \hat{y}k_y^i$, $\bar{k}_r = \hat{x}k_x^r + \hat{y}k_y^r$, and R is the reflection coefficient) for incident and reflected waves, respectively.

On the PMC surface, the tangential component of magnetic field vanishes, and then we get $H_x^i|_{y=0} + H_x^r|_{y=0} = 0$ or, in detail, $(k_y^i - ik_0\chi)\, e^{i\bar{k}_i\cdot\bar{r}}|_{y=0} = -R(k_y^r - ik_0\chi)\, e^{i\bar{k}_r\cdot\bar{r}}|_{y=0}$. Phase matching on the surface requires $k_x^i = k_x^r = k_x$, and we get

$$R = -\frac{k_y^i - ik_0\chi}{k_y^r - ik_0\chi} \tag{6}$$

We emphasize that the incident and reflected T-spin beams are linked through their magnetic fields, as enforced by the boundary condition of the PMC that the tangential **H** field must vanish at the interface. As such, the reflection coefficient is related to the T-spin

formed by the magnetic field of the photons. On the other hand, if the reflector is replaced by a PEC, then $R = -1$ holds for arbitrary incidence. In such a case, there would be no shift in the center of the reflected beam because the magnetic T-spin is not involved in the boundary condition. Hence, we study the reflection from a PMC surface to guarantee the geometrodynamic nature of the problem.

To show the geometrical dynamics of the reflection, we assume that the elliptically polarized incident and reflected waves are written as $\overline{H}_i = U_i(\hat{x} + \hat{y}\,A_i e^{iQ_i})\,e^{i\overline{k}_i\cdot\overline{r}}$ and $\overline{H}_r = U_r(\hat{x} + \hat{y}\,A_r e^{iQ_r})\,e^{i\overline{k}_r\cdot\overline{r}}$, wherein A and Q are two real factors to handle the T-spinning, i.e., with nonzero A, Q is crucial in generating the spinning (*5*). For incident and reflected waves, A_i (Q_i) and A_r (Q_r) generally differ and can be determined by consulting their wave vectors ($\overline{k}_i$ and $\overline{k}_r$). For instance, the magnetic field of incident and reflected waves can be simply expressed through their eigenstates, i.e., $\overline{H}_i = H_0\hat{h}_i e^{i\overline{k}_i\cdot\overline{r}}$ and $\overline{H}_r = RH_0\hat{h}_r e^{i\overline{k}_r\cdot\overline{r}}$, with $\hat{h}_i$ and $\hat{h}_r$ being the normalized magnetizations. It is straightforward to have $A_i e^{iQ_i} = \frac{h_{y,i}}{h_{x,i}}$ and $A_r e^{iQ_r} = \frac{h_{y,r}}{h_{x,r}}$. By matching the tangential continuity on the PMC surface, we can simply establish the relationship between incident and reflected waves as $R = -\frac{h_{x,i}}{h_{x,r}}$.

Physically, R plays the role of connection between incident and reflected waves, which contains all the information needed in describing the variation of the T-spin photon (TSP). To illustrate the change of T-spin states in the interaction, R is rewritten as

$$R = -\frac{h_{x,i}}{h_{y,i}}\cdot\frac{h_{y,r}}{h_{x,r}}\cdot\frac{h_{y,i}}{h_{y,r}} = -\frac{A_r e^{iQ_r}}{A_i e^{iQ_i}} \tag{7}$$

It reveals that the transition of the T-spin state gives rise to an extra phase delay to the TSP's propagation, i.e., $Q_r - Q_i$, which is of spinning nature and will be lifted for linearly magnetized waves.

T-spin induced beam shifts

From previous analysis, TSPs experience a phase delay, i.e., $P(\phi_i,\phi_r)$, in the reflection because of the variation of T-spin states. With varying the incident angle, this phase changes. Numerically, the beam shift can be found out through calculating the directional derivative of the phase of reflectance. For instance, $D_x = \frac{dP}{dk_x}$ represents the spatial shift of light beams in $\hat{x}$ direction. For $R = e^{iP(\phi_i,\phi_r)}$, we get $D_x = -iR^{-1}\cdot\frac{dR}{dk_x}$. By using Eq. 6, we obtain

$$D_x = -i\frac{-\frac{dk_{y,i}}{dk_x}}{-k_{y,i} + ik_0\chi} + i\frac{-\frac{dk_{y,r}}{dk_x}}{-k_{y,r} + ik_0\chi}$$

For $\frac{\mu_1}{\mu_2}k_x^2 + k_y^2 = k_0^2(\varepsilon_3\mu_1 - \chi^2)$, we have $-\frac{dk_{y,i(r)}}{dk_x} = \frac{\mu_1}{\mu_2}\frac{k_x}{k_{y,i(r)}}$. In addition, noticing that $k_{y,i} = -k_{y,r}$ and $(k_{y,i})^2 = (k_{y,r})^2 = k_y^2$, D_x can be rewritten as $D_x = -2\frac{k_0}{k_{y,i}}\frac{\mu_1}{\mu_2}\frac{\chi k_x}{k_y^2 + k_0^2\chi^2}$. It is obvious that D_x is induced by nonzero χ, and the shifting will be reversed if χ takes an opposite sign.

Now, we are ready to find out the inner connection between the SAM and the spin Hall–induced beam shift. The SAM of the bulk mode with magnetic T-spin can be worked out through $\overline{S} = \mathrm{Im}[\mu_0\overline{H}^*\times\overline{H}]/4\omega$ (*4*), which leads to $\overline{S} = \hat{z}\frac{-\mu_0}{2c}|H_x|^2\frac{\mu_1}{\mu_2}\frac{\chi k_x}{k_y^2 + k_0^2\chi^2}$, where c is the speed of light in the free space. It is obvious that $\overline{S}_i = \overline{S}_r$ because $H_{x,i} = H_{x,r} \neq 0$. For T-spin light with predefined H_x, we can define a normalized SAM as $\overline{S}^n = \frac{\overline{S}}{|H_x|^2} = \hat{z}\frac{-\mu_0}{2c}\frac{\mu_1}{\mu_2}\frac{\chi k_x}{k_y^2 + k_0^2\chi^2}$. Then, D_x can be expressed (in the form of $\overline{S}^n$) as $D_x = 4c\frac{k_0}{\mu_0 k_{y,i}}(\hat{z}\cdot\overline{S}^n)$.

Numerical estimation of the beam center

In the simulations, E_z distributions are obtained in the zone close to the PMC surface. To observe the spin Hall–induced beam shift, the position of the center of the reflected beam shall be extracted. To this end, we determine the intensity of E_z by extracting its absolute value, as shown in fig. S1 (A and B). Then, we obtain the $|E_z|$ distribution in a cutting plane normal to the reflected wave vector ($\overline{k}_r$). The position of the cutting plane is highlighted in red in fig. S1 (A and B). A typical $|E_z|$ distribution in the cutting plane is exhibited in fig. S1C. The position of the beam center is obtained by evaluating $\mathrm{BC} = \frac{\int|E_z|x\,dx}{\int|E_z|\,dx}$, where the integral path is along the cutting plane. In simulations, if $\chi = 0$, i.e., no spin Hall shift is induced, then the beam center reference ($\mathrm{BC}^{\mathrm{ref}}$) is obtained. With nonzero χ, the beam center shifted by spin Hall effect is obtained as BC^{χ}. Then, the shift distance is derived by comparing the beam centers for two cases, i.e., $D_t^{\chi} = \mathrm{BC}^{\chi} - \mathrm{BC}^{\mathrm{ref}}$.

MM design

MMs consisting of single-gap split-ring resonators (SRRs) can be designed to have the required bianisotropic EM parameters, as shown in fig. S2A. To reduce the overall dimension of a single unit cell, the two arms of the SRR (SRR I) are bent into curved shape, as shown in fig. S2B. Thus, the size of the unit cell can be much smaller than the free space wavelength. However, such an MM is still anisotropic because of the lack of rotational symmetry, and hence, the refraction index in x and y directions would be different. It is highly desired that the MM exhibits isotropic spatial dispersion in the x-y plane, because material anisotropy would complicate the T-spin–induced phenomenon. To this end, a secondary SRR (SRR II; oriented perpendicular to SRR I) is introduced to provide an additional degree of freedom to tune μ_x (or equivalently, y direction refractive index), as shown in fig. S2 (C and D). The overall unit cell of our MM is constructed by combining SRR I and SRR II, on a printed circuit board substrate (composed of poly tetra fluoroethylene and glass fibres, with $\varepsilon_r = 2.55$ and loss tangent of 0.003), as the supporting substrate. Please refer to fig. S2 (E to G) for details.

Note that, by bending the metallic arms of both SRRs I and II, some unwanted ME effects would be induced. For instance, SRR I exhibits ME coupling not only between E_z and H_y but also between E_z and H_z. Similar ME coupling also exists in SRR II. Here, a single layer of the MM unit cells is sandwiched between two PEC plates along z direction, and the implementation of PEC boundary condition on both sides can suppress these unwanted effects. For the numerical calculation of the band dispersion, periodic boundary condition is applied in both x and y directions, and PEC ($E_t = 0$) bounds are set at $Z_{\max}$ and $Z_{\min}$. The reason to have such boundary confinement in z direction is twofold. First, we are focusing on the TE polarization for which the electric field is z-polarized. Second, all the unwanted ME coupling brought by the bending arms of the SRRs are eliminated from a macroscopic view.

Last, by tuning the dimensions of SRRs I and II, a bianisotropic MM with nearly isotropic spatial dispersion (in the x-y plane) can

be obtained, as shown in fig. S3. For the detailed information about the structural parameters, please refer to the figure captions. Here, in fig. S3, we show the band structure and three equifrequency contours of the MM. It is obvious that the MM exhibits near isotropic spatial dispersion in the range between 9.5 and 10.5 GHz. Furthermore, if we consider the small size of the unit cell, then it is evident that such an MM can behave as a homogeneous medium in the band of interest. Here, by using the reflection/transmission coefficients (the *S* parameters), the effective constitutive parameters (ε_z, μ_x, μ_y, and χ) relevant to the TE polarized waves are retrieved through the algorithm reported in (*43*–*45*), which are shown in Fig. 3.

In the experiments, we can obtain the transmission spectra for the fabricated MM in orthogonal directions, as shown in fig. S4. It shows that the fabricated MM has a transmission band of more than 8.7 GHz in both the *x* and *y* directions, which confirms our design and fabrication. The fluctuation between the two transmittance curves is induced because of the distinct impedances of the MM along these two directions.

Experimental setup

To facilitate the experimental measurements, we combine two quarter circular-shaped samples, as shown in fig. S5. The radii of the two circles are $R_1 = 60$ cm and $R_2 = 90$ cm, respectively. The EM wave is excited from the small quarter circle and is detected at the edge of the big one, as indicated by the red and purple arrows in fig. S5, respectively. The incident beam is launched by a standard horn antenna, whose main lobe points to the origin of the quarter circle(s). We design the sample in such a configuration for two reasons. First, a smaller quarter circle in the incident side can help reduce the broadening of EM beams. Second, a larger quarter circle in the receiving side can help minimize the edge effect that may affect the EM beams with a broad beam width. Because the beam shift (D_t) is much smaller than R_2, we simply have $D_t \approx R_2\varphi_s$.

AMR design

The design of the AMR, as shown in fig. S6 (A to C), consists of two single-turn helices of different shapes combined together. The structure is embedded into an F4B substrate to form the final unit cell, as shown in fig. S6 (D to E). The helical structure of the unit cell can excite ME coupling between H_y and E_y, i.e., a chiral response, which is not desired by the AMR. To eliminate the unwanted ME coupling (chirality), PEC boundary condition ($\overline{E}_t = 0$) is implemented at Z_{max} and Z_{min}.

Because of the strong magnetic response of the helical unit cell, the AMR is expected to have PMC-like reflection at frequencies where the internal magnetic resonance takes place, i.e., the frequency region with extremely large effective permeability. However, it is rather hard and almost impossible to make an accurate estimation of the permeability in the AMR's resonance frequency region because complex coupling may exist and the spatial dispersion (nonlocal effect) may dominate the macroscopic EM behaviors of the AMR. Nevertheless, we only need to focus on the AMR's reflection behavior, so the AMR's reflectance is sufficient to characterize its particular role as a magnetic reflector. Here, with full-wave simulation, we obtain the phase of reflectance from the AMR for several oblique illumination angles, as shown in fig. S7A. It is obvious that the phases of reflectance at different incident angles from the AMR surface are almost identical to a value close to zero at around 9.75, and a PMC-like behavior is confirmed. This phenomenon occurs because of the enhanced magnetic permeability in the *y* direction, as expected. On the basis of the reflection/transmission coefficients and by applying the retrieval method proposed in (*46*), we make an estimation of the AMR's effective parameters (by neglecting the spatial dispersion), which are shown in fig. S7 (B and C). It is confirmed that the magnetic permeability is substantially enhanced at around 9.75 GHz.

In the experiments, we measure the transmission and reflection from the AMR sample. The measurement configuration is shown in fig. S8A, wherein the reflection is measured by two horn antennas (a transmitter and a receiver) in an open environment. For the AMR, we find that the transmission is extremely weak (the transmission power level cannot be identified from the environment noise) in the band above 9.5 GHz, so only the reflection spectrum is shown in fig. S8 (C and D). It is shown that, although the measured reflected power is lower than that of the simulation due to the collection loss, the spectral distribution can roughly match the simulated results.

Implementation of the PMC boundary

In previous discussion, we show that PMC is required for the demonstration of the T-spin–induced Hall effect. Here, we show that a PMC-like boundary can be provided by an anisotropic MM with extreme parameters. We consider the refraction from the interface between a bianisotropic medium and an anisotropic medium, as shown in fig. S9.

The incident and reflected waves in region I can be expressed by $\begin{bmatrix} h_{x,i} \\ h_{y,i} \\ e_{z,i} \end{bmatrix} e^{i\overline{k}_i\cdot\overline{r}} = \begin{bmatrix} \frac{1}{\omega\mu_0\mu_1}(k_{y,i} - ik_0\chi) \\ \frac{1}{\omega\mu_0\mu_1}\left(-\frac{\mu_1}{\mu_2}k_x\right) \\ 1 \end{bmatrix} e^{i\overline{k}_i\cdot\overline{r}}$ and $\begin{bmatrix} h_{x,r} \\ h_{y,r} \\ e_{z,r} \end{bmatrix} e^{i\overline{k}_r\cdot\overline{r}} = R\begin{bmatrix} \frac{1}{\omega\mu_0\mu_1}(k_{y,r} - ik_0\chi) \\ \frac{1}{\omega\mu_0\mu_1}\left(-\frac{\mu_1}{\mu_2}k_x\right) \\ 1 \end{bmatrix} e^{i\overline{k}_r\cdot\overline{r}}$, with $\frac{\mu_1}{\mu_2}k_x^2 + k_y^2 = k_0^2(\varepsilon_3\mu_1 - \chi^2)$. For the transmitted wave in region II, we have $\begin{bmatrix} h_{x,t} \\ h_{y,t} \\ e_{z,t} \end{bmatrix} e^{i\overline{k}_t\cdot\overline{r}} = T\begin{bmatrix} \frac{1}{\omega\mu_0\mu_x}k_{y,t} \\ \frac{-1}{\omega\mu_0\mu_y}k_{x,t} \\ 1 \end{bmatrix} e^{i\overline{k}_t\cdot\overline{r}}$ with $k_x^2 + \frac{\mu_y}{\mu_x}k_y^2 = k_0^2\varepsilon_z\mu_y$.

The continuity of the tangential electric and magnetic fields leads to

$$1 + R = T$$
$$\frac{1}{\mu_1}(k_{y,i} - ik_0\chi) + \frac{R}{\mu_1}(k_{y,r} - ik_0\chi) = \frac{T}{\mu_x}k_{y,t}$$

Thus, it follows that

$$R = -\frac{\left(\frac{k_{y,i}}{k_0} - i\chi\right) - \frac{\mu_1 k_{y,t}}{\mu_x k_0}}{\left(\frac{k_{y,r}}{k_0} - i\chi\right) - \frac{\mu_1 k_{y,t}}{\mu_x k_0}} \tag{8}$$

We note that Eq. 8 will return to Eq. 6 if region II is really filled by a PMC. Nevertheless, the PMC-like reflectance can still be achieved by $\frac{\mu_1 k_{y,t}}{\mu_x k_0} \to 0$, even without a real PMC. This condition can be satisfied if μ_x is sufficiently large and any other parameters are kept finite, i.e., $\left|\frac{\mu_1 k_{y,t}}{\mu_x k_0}\right|_{\mu_x\to\infty} = \left|\frac{\mu_1}{k_0}\sqrt{\frac{k_0^2\varepsilon_z\mu_y - k_x^2}{\mu_x\mu_y}}\right|_{\mu_x\to\infty} \to 0$. For practical

implementations, medium of this kind may be designed on the basis of standard SRRs or helical structures. For instance, if $\left|\frac{\mu_1 k_{y,t}}{\mu_x k_0}\right|$ is small enough, then we can rewrite Eq. 8 as

$$R = -\frac{A_1}{A_2}\cdot\frac{1-\frac{\mu_1}{A_1\mu_x}k_{y,t}}{1-\frac{\mu_1}{A_2\mu_x}k_{y,t}} \tag{9}$$

with $A_1 = k_{y,i} - ik_0\chi$ and $A_2 = k_{y,r} - ik_0\chi$. It is straightforward to obtain $R \approx -\frac{A_1}{A_2}$, provided by $\left|\frac{\mu_1}{A_j\mu_x}k_{y,t}\right| \ll 1$ (j = 1,2). With $k_{y,i} = -k_{y,r}$, $A_1 = k_{y,i} - ik_0\chi$, and $A_2 = -k_{y,i} - ik_0\chi$, we get

$$\left|\frac{\mu_1}{A_j\mu_x}k_{y,t}\right|_{j=1,2} = \frac{1}{\sqrt{\left(\frac{k_{y,i}}{k_0}\right)^2+\chi^2}}\left|\frac{\mu_1 k_{y,t}}{\mu_x k_0}\right| \tag{10}$$

Because $\frac{k_{y,i}}{k_0}$ is always finite and real, $\left|\frac{\mu_1}{A_j\mu_x}k_{y,t}\right| \ll 1$ could be ensured by $\left|\frac{\mu_1 k_{y,t}}{\mu_x k_0}\right| \ll |\chi|$. We note that this condition can be fulfilled at frequencies close to the MM's resonance.

On the other hand, the beam shift can be observed by measuring the relative difference between the beam shifts of optical modes with opposite T-spin feature, by using MMs with opposite bianisotropy, i.e., χ and $-\chi$. For simplicity, we neglect the surface loss and assume $R = e^{iP}$, then we have $\Delta_x = D_x^{\chi} - D_x^{-\chi}$ with $D_x = \frac{dP}{dk_x}$. The relative beam shift can be further derived as $\Delta_x = \frac{d(P_x^{\chi} - P_x^{-\chi})}{dk_x} = \frac{-i}{(R^{\chi}/R^{-\chi})}\frac{d(R^{\chi}/R^{-\chi})}{dk_x}$. Thus, the key term in determining Δ_x is $R_\Delta = R^{\chi}/R^{-\chi}$. In practice, the measurement of R_Δ is more robust than R^{χ} (or $R^{-\chi}$), considering the systematic uncertainties. From Eq. 9, we obtain

$$R_\Delta = \frac{R^{\chi}}{R^{-\chi}} = \left(\frac{A_1}{A_2}\right)^2\cdot\frac{1-\frac{\left(\frac{k_{y,i}}{k_0}+i\chi\right)^2\left(\frac{\mu_1 k_{y,t}}{\mu_x k_0}\right)^2}{\left[\left(\frac{k_{y,i}}{k_0}\right)^2+\chi^2\right]\left[\left(\frac{k_{y,i}}{k_0}\right)^2+\chi^2\right]}}{1-\frac{\left(\frac{k_{y,i}}{k_0}-i\chi\right)^2\left(\frac{\mu_1 k_{y,t}}{\mu_x k_0}\right)^2}{\left[\left(\frac{k_{y,i}}{k_0}\right)^2+\chi^2\right]\left[\left(\frac{k_{y,i}}{k_0}\right)^2+\chi^2\right]}}$$

$$= \left(\frac{A_1}{A_2}\right)^2\cdot\frac{1-\frac{\left(\frac{k_{y,i}}{k_0}+i\chi\right)^2}{\left[\left(\frac{k_{y,i}}{k_0}\right)^2+\chi^2\right]}\cdot\left|\frac{\mu_1}{A_1\mu_x}k_{y,t}\right|^2}{1-\frac{\left(\frac{k_{y,i}}{k_0}-i\chi\right)^2}{\left[\left(\frac{k_{y,i}}{k_0}\right)^2+\chi^2\right]}\cdot\left|\frac{\mu_1}{A_2\mu_x}k_{y,t}\right|^2}$$

Because $\left|\frac{\left(\frac{k_{y,i}}{k_0}\pm i\chi\right)^2}{\left[\left(\frac{k_{y,i}}{k_0}\right)^2+\chi^2\right]}\right| \le 1$, it is evident that R_Δ would be less perturbed than R^{χ} (a numerical comparison can be found in fig. S10), provided $|\frac{\mu_1}{A_j\mu_x}k_{y,t}|$ is sufficiently small, or equivalently $\left|\frac{\mu_1 k_{y,t}}{\mu_x k_0}\right| \ll |\chi|$. Here, with the effective parameters of both the bianisotropic MM (Fig. 3) and the AMR (fig. S7), we can evaluate the ratio between $|\chi|$ and $|\frac{\mu_1 k_{y,t}}{\mu_x k_0}|$, as shown in fig. S9B. It is evident that around 9.75 GHz, the ratio is enhanced $\left(|\chi|/\left|\frac{\mu_1 k_{y,t}}{\mu_x k_0}\right| > 10\right)$, and AMR can behave like a PMC regardless of the incident angle.

SUPPLEMENTARY MATERIALS

Supplementary material for this article is available at https://science.org/doi/10.1126/sciadv.abo6033

REFERENCES AND NOTES

1. A. I. Akhiezer, V. B. Berestetskii, *Quantum Electrodynamics* (Interscience Publishers, 1965).
2. A. Bérard, H. Mohrbach, Spin hall effect and Berry phase of spinning particles. *Phys. Lett. A* **352**, 190–195 (2006).
3. K. Y. Bliokh, A. Aiello, M. A. Alonso, Quantum electrodynamics, angular momentum and chirality, *The Angular Momentum of Light*, D. L. Andrews, M. Babiker, Eds. (Cambridge Univ. Press, 2012).
4. A. Aiello, P. Banzer, M. Neugebaueru, G. Leuchs, From transverse angular momentum to photonic wheels. *Nat. Photon.* **9**, 789–795 (2015).
5. K. Y. Bliokh, F. Nori, Transverse and longitudinal angular momenta of light. *Phys. Rep.* **592**, 1–38 (2015).
6. L. Marrucci, E. Karimi, S. Slussarenko, B. Piccirillo, E. Santamato, E. Nagali, F. Sciarrino, Spin-to-orbital conversion of the angular momentum of light and its classical and quantum applications. *J. Opt.* **13**, 064001 (2011).
7. K. Y. Bliokh, M. A. Alonso, E. A. Ostrovskaya, A. Aiello, Angular momenta and spin-orbit interaction of nonparaxial light in free space. *Phys. Rev. A* **82**, 63825 (2010).
8. K. Y. Bliokh, A. Niv, V. Kleiner, E. Hasman, Geometrodynamics of spinning light. *Nat. Photon.* **2**, 748–753 (2008).
9. S. J. van Enk, G. Nienhuis, Spin and orbital angular momentum of photons. *Europhys. Lett.* **25**, 497–501 (1994).
10. F. Alpeggiani, K. Y. Bliokh, F. Nori, L. Kuipers, Electromagnetic helicity in complex media. *Phys. Rev. Lett.* **120**, 243605 (2018).
11. K. Y. Bliokh, F. J. Rodríguez-Fortuño, F. Nori, A. V. Zayats, Spin–orbit interactions of light. *Nat. Photon.* **9**, 796–808 (2015).
12. K. Y. Bliokh, E. A. Ostrovskaya, M. A. Alonso, O. G. Rodríguez-Herrera, D. Lara, C. Dainty, Spin-to-orbital angular momentum conversion in focusing, scattering, and imaging systems. *Opt. Express* **19**, 26132–26149 (2011).
13. Y. Zhao, J. S. Edgar, G. D. M. Jeffries, D. McGloin, D. T. Chiu, Spin-to-orbital angular momentum conversion in a strongly focused optical beam. *Phys. Rev. Lett.* **99**, 073901 (2007).
14. Y. Gorodetski, A. Niv, V. Kleiner, E. Hasman, Observation of the spin-based plasmonic effect in nanoscale structures. *Phys. Rev. Lett.* **101**, 043903 (2008).
15. A. Ciattoni, G. Cincotti, C. Palma, Angular momentum dynamics of a paraxial beam in a uniaxial crystal. *Phys. Rev. E* **67**, 36618 (2003).
16. A. B. Khanikaev, S. H. Mousavi, W.-K. Tse, M. Kargarian, A. H. MacDonald, G. Shvets, Photonic topological insulators. *Nat. Mater.* **12**, 233–239 (2013).
17. F. D. M. Haldane, S. Raghu, Possible realization of directional optical waveguides in photonic crystals with broken time-reversal symmetry. *Phys. Rev. Lett.* **100**, 013904 (2008).
18. M. C. Rechtsman, J. M. Zeuner, Y. Plotnik, Y. Lumer, D. Podolsky, F. Dreisow, S. Nolte, M. Segev, A. Szameit, Photonic Floquet topological insulators. *Nature* **496**, 196–200 (2013).
19. S. H. Gong, F. Alpeggiani, B. Sciacca, E. C. Garnett, L. Kuipers, Nanoscale chiral valley-photon interface through optical spin-orbit coupling. *Science* **359**, 443–447 (2018).
20. P. Lodahl, S. Mahmoodian, S. Stobbe, A. Rauschenbeutel, P. Schneeweiss, J. Volz, H. Pichler, P. Zoller, Chiral quantum optics. *Nature* **541**, 473–480 (2017).
21. R. Mitsch, C. Sayrin, B. Albrecht, P. Schneeweiss, A. Rauschenbeutel, Quantum state-controlled directional spontaneous emission of photons into a nanophotonic waveguide. *Nat. Commun.* **5**, 5713 (2014).
22. F. J. Rodríguez-Fortuño, G. Marino, P. Ginzburg, D. O'Connor, A. Martínez, G. A. Wurtz, A. V. Zayats, Near-field interference for the unidirectional excitation of electromagnetic guided modes. *Science* **340**, 328–330 (2013).
23. M. Onoda, S. Murakami, N. Nagaosa, Hall effect of light. *Phys. Rev. Lett.* **93**, 083901 (2004).
24. O. Hosten, P. Kwiat, Observation of the spin Hall effect of light via weak measurements. *Science* **319**, 787–790 (2008).
25. X. Yin, Z. Ye, J. Rho, Y. Wang, X. Zhang, Photonic spin hall effect at metasurfaces. *Science* **339**, 1405–1407 (2013).
26. K. Y. Bliokh, Y. Gorodetski, V. Kleiner, E. Hasman, Coriolis effect in optics: Unified geometric phase and spin-Hall effect. *Phys. Rev. Lett.* **101**, 030404 (2008).
27. A. Aiello, J. P. Woerdman, Role of beam propagation in Goos–Hänchen and Imbert–Fedorov shifts. *Opt. Lett.* **33**, 1437–1439 (2008).
28. K. Y. Bliokh, A. Aiello, Goos–Hänchen and Imbert–Fedorov beam shifts: An overview. *J. Opt.* **15**, 014001 (2013).
29. F. I. Fedorov, To the theory of total reflection. *J. Opt.* **15**, 014002 (2013).
30. K. Y. Bliokh, D. Smirnova, F. Nori, Quantum spin Hall effect of light. *Science* **348**, 1448–1451 (2015).
31. M. Antognozzi, C. R. Bermingham, R. L. Harniman, S. Simpson, J. Senior, R. Hayward, H. Hoerber, M. R. Dennis, A. Y. Bekshaev, K. Y. Bliokh, F. Nori, Direct measurements of the extraordinary optical momentum and transverse spin-dependent force using a nano-cantilever. *Nat. Phys.* **12**, 731–735 (2016).
32. M. Neugebauer, J. S. Eismann, T. Bauer, P. Banzer, Magnetic and electric transverse spin density of spatially confined light. *Phys. Rev. X* **8**, 021042 (2018).

33. A. Y. Bekshaev, K. Y. Bliokh, F. Nori, Transverse spin and momentum in two-wave interference. *Phys. Rev. X* **5**, 011039 (2015).
34. J. S. Eismann, L. H. Nicholls, D. J. Roth, M. A. Alonso, P. Banzer, F. J. Rodríguez-Fortuño, A. V. Zayats, F. Nori, K. Y. Bliokh, Transverse spinning of unpolarized light. *Nat. Photon.* **15**, 156–161 (2021).
35. L. Peng, L. Duan, K. Wang, F. Gao, L. Zhang, G. Wang, Y. Yang, H. Chen, S. Zhang, Transverse photon spin of bulk electromagnetic waves in bianisotropic media. *Nat. Photon.* **13**, 878–882 (2019).
36. K. Y. Bliokh, A. Y. Bekshaev, F. Nori, Extraordinary momentum and spin in evanescent waves. *Nat. Commun.* **5**, 3300 (2014).
37. J. D. Jackson, *Classical Electrodynamics* (John Wiley & Sons Inc., 1975).
38. P. Lodahl, S. Mahmoodian, S. Stobbe, Interfacing single photons and single quantum dots with photonic nanostructures. *Rev. Mod. Phys.* **87**, 347–400 (2015).
39. Y. Wang, H. Li, Z. Cao, T. Yu, Q. Shen, Y. He, Oscillating wave sensor based on the Goos-Hänchen effect. *Appl. Phys. Lett.* **92**, 061117 (2008).
40. D. Xu, S. He, J. Zhou, S. Chen, S. Wen, H. Luo, Goos–Hänchen effect enabled optical differential operation and image edge detection. *Appl. Phys. Lett.* **116**, 211103 (2020).
41. S. He, J. Zhou, S. Chen, W. Shu, H. Luo, S. Wen, Wavelength-independent optical fully differential operation based on the spin-orbit interaction of light. *APL Photon.* **5**, 036105 (2020).
42. J. A. Kong, *Electromagnetic Wave Theory* (EMW Publishing, 2005).
43. L. Peng, X. Zheng, K. Wang, S. Sang, Y. Chen, G. Wang, Layer-by-layer design of bianisotropic metamaterial and its homogenization. *Prog. Electromagn. Res.* **159**, 39–47 (2017).
44. Z. Li, K. Aydin, E. Ozbay, Determination of the effective constitutive parameters of bianisotropic metamaterials from reflection and transmission coefficients. *Phys. Rev. E* **79**, 026610 (2009).
45. X. Chen, T. M. Grzegorczyk, B.-I. Wu, J. Pacheco, J. A. Kong, Robust method to retrieve the constitutive effective parameters of metamaterials. *Phys. Rev. E* **70**, 016608 (2004).
46. C. Menzel, C. Rockstuhl, T. Paul, F. Lederer, T. Pertsch, Retrieving effective parameters for metamaterials at oblique incidence. *Phys. Rev. B* **77**, 195328 (2008).

Acknowledgments

Funding: This work is financially supported by the Natural Science Foundation of China (NSFC) under grants 61875051, 61805097, and 61935015; the Natural Science Foundation of Zhejiang Province (ZJNSF) under grant LR21F010002; and the Hong Kong RGC (AoE/P-502/20, 17309021). **Author contributions:** Conceptualization: L.P. and S.Z. Methodology: L.P., H.R., Y.-C.L., S.X., H.-S.C., and S.Z. Data curation: L.P., H.R., T.-W.L., and K.-W.X. Validation: L.P., D.-X.Y., H.-B.S., and S.Z. Supervision: L.P., S.X., and S.Z. Writing—original draft: L.P. and S.X. Writing—review and editing: L.P. and S.Z. **Competing interests:** The authors declare that they have no competing interests. **Data and materials availability:** All data needed to evaluate the conclusions in the paper are present in the paper and/or the Supplementary Materials.

Submitted 14 February 2022
Accepted 14 July 2022
Published 26 August 2022
10.1126/sciadv.abo6033